CHARACTERIZING THE SOLAR WIND-MAGNETOSPHERE VISCOUS INTERACTION

IN THE OUTER SOLAR SYSTEM:

ANALYTICAL ASSESSMENT OF THE PROBABILITY OF THE KELVIN HELMHOLTZ

INSTABILITY GROWTH AT URANUS AND NEPTUNE

by

ANGELA J. OLSEN

A THESIS

Presented to the Department of Earth Sciences
and the Division of Graduate Studies of the University of Oregon
in partial fulfillment of the requirements
for the degree of
Master of Science

December 2021

THESIS APPROVAL PAGE

Student: Angela J. Olsen

Title: Characterizing the Solar Wind-Magnetosphere Viscous Interaction in the Outer Solar System: Analytical Assessment of the Probability of the Kelvin-Helmholtz Instability Growth at Uranus and Neptune

This thesis has been accepted and approved in partial fulfillment of the requirements for the Master of Science degree in the Department of Earth Sciences by:

Carol Paty	Chair
Josef Dufek	Member
Alan Rempel	Member
Dean Livelybrooks	Institutional Representative

and

Krista Chronister	Vice Provost for Graduate Studies

Original approval signatures are on file with the University of Oregon Division of Graduate Studies.

Degree awarded December 2021

THESIS ABSTRACT

Angela J. Olsen

Master of Science

Department of Earth Science

December 2021

Title: Characterizing the Solar Wind-Magnetosphere Viscous Interaction in the Outer Solar System: Analytical Assessment of the Probability of the Kelvin-Helmholtz Instability Growth at Uranus and Neptune

Uranus and Neptune have dynamic magnetopause interfaces to the solar wind due to the orientation of their rotation and magnetic axes. The magnetohydrodynamic plasma description suggests that solar wind conditions in the outer solar system encourage magnetosphere boundaries at Uranus and Neptune to be more Kelvin-Helmholtz (KH) unstable, but no quantitative assessment has been performed. This study employs an analytical model to test the condition for KH instability growth at the outermost planets in the solar system. The solar wind and tilted planetary magnetic field are separated by a surface representing the magnetopause. Values from each region are applied to the KH condition to evaluate if the instability is possible. The model is evaluated for both Uranus and Neptune at solstice and equinox geometries, under a variety of solar wind interplanetary magnetic fields, and over the course of its daily rotation.

CURRICULUM VITAE

NAME OF AUTHOR: Angela J. Olsen

GRADUATE AND UNDERGRADUATE SCHOOLS ATTENDED:

University of Oregon, Eugene
University of California, Santa Barbara

DEGREES AWARDED:

Master of Science, Earth Science, 2021, University of Oregon
Bachelor of Science, 2019, Physics, University of California, Santa Barbara
Bachelors Minor, 2019, Earth Science, University of California, Santa Barbara

AREAS OF SPECIAL INTEREST:

Space Plasma Physics
Planetary Science

PROFESSIONAL EXPERIENCE:

Undergraduate research assistant, Department of Geology, University at Buffalo, 2018

Undergraduate peer advisor, Department of Physics, University of California, Santa Barbara, 2018-2019

Technical mentor, Center for Science and Engineering Partnerships, University of California, Santa Barbara, 2019

Teaching assistant, Department of Earth Science, University of Oregon, Eugene, 2019-2021

GRANTS, AWARDS, AND HONORS:

NASA Heliophysics Summer School, University Corporation for Atmospheric Research, Boulder (Virtual), 2020

Johnston Travel Award, Department of Earth Science, University of Oregon, Eugene, 2019

Chair's Appreciation Award, Department of Physics, University of California, Santa Barbara, 2019

ACKNOWLEDGEMENTS

For my parents Karl and Laura who taught me the best lessons in life: to be kind and to be curious. And for my closest and dearest friends Lauren, Morgan, Madison, Kirk, Evan, Madeleine, Fiona, Kylene, Lydia, Jenna, Arlo, and Dom for bringing light and love to my life when I needed it most. I can never thank you enough.

TABLE OF CONTENTS

LIST OF FIGURES

LIST OF TABLES

I. INTRODUCTION

The solar wind encounters and interacts with various planetary bodies as it flows outward and expands towards the edge of the solar system, producing a wide range of interaction structures which are governed by the characteristics of the planet and local solar wind. When encountering magnetized planets or planets with a substantial atmosphere and ionosphere, a shock will form from the super magnetosonic solar wind running into a magnetic obstacle. When it encounters planets without global magnetic fields (Venus, Mars, Pluto) the solar wind interacts with the upper atmosphere by heating and accelerating charged particles, giving them energy to escape (Futaana, 2017; Lillis, 2015; McComas, 2016). If the solar wind interacts with an object without an atmosphere or global magnetic field (such as the Moon), it will bombard the surface of the body and sputter the soil to chemically alter its composition or electrostatically loft particles (Dukes, 1991; Poppe, 2014; Szalay, 2015). In some cases, the solar wind interaction with a global magnetic field can lead to magnetic reconnection that drives magnetospheric convection or lead to a viscous interaction which can occur at the magnetopause boundary between the shocked solar wind and the magnetospheric plasma (Masters, 2018). Viscous solar wind-magnetosphere interaction is significantly enhanced by the growth of the Kelvin Helmholtz Instability (KHI) at the magnetopause boundary (Axford, 1964).

The Kelvin-Helmholtz instability (KHI) occurs when there is a velocity shear across the interface between two fluids. Space plasmas can be modeled as compressible conducting fluids using the magnetohydrodynamic formulation (Chandrasekhar, 1961), allowing us to represent solar wind plasma and magnetospheric plasma as two interacting fluids separated by the magnetopause boundary. Viscous interaction between the solar wind and magnetospheric plasma occurs because the KHI allows for plasma mixing and energy transfer through Kelvin Helmholtz (KH) waves and vortices. Localized regions of magnetic reconnection can occur in KH vortices, creating an intermittent mode of plasma transport very different from the plasma transport of global magnetic reconnection (Delamere, 2011; Masters, 2018). The probability of global magnetic reconnection drops with increasing heliospheric distance as the density and magnetic field strength of the solar wind decrease. Conversely, the probability of the KHI rises with increasing heliospheric distance as weaker IMF and more dilute plasma increase the potential for viscous interaction (Masters, 2018). The KHI occurs as the result of a velocity shear across the magnetopause boundary, and the likelihood of the KHI also depends on the relative orientation of the magnetospheric field to that of the draped solar wind magnetic field at the magnetopause interface. This makes planets with asymmetric and dynamic magnetospheric geometries interesting environments to study the KHI (Paty et al., 2020; Gershman & DiBraccio, 2020).

In 1986 and 1989, Voyager 2 flew through Uranus and Neptune's magnetospheres, respectively, and recorded how the geometry of both planet's magnetic and rotation axes create a more dynamic magnetospheric system than we have at Earth. At Uranus, the magnetic moment is tilted relative to the rotation axis by 60 degrees, and the rotation axis is tilted -97.8 degrees relative to the normal of the ecliptic (Figure 1) (Ness et al., 1986). At Neptune, the magnetic moment is tilted relative to the rotation axis by 47 degrees, and the rotation axis is tilted 23 degrees relative to the normal of the ecliptic (Figure 1) (Ness et al., 1989). The axes at Uranus and Neptune create significant changes in the orientations of the velocity and magnetic field vectors, as well as the magnetospheric density, all of which together determine the probability of the KHI occurring along the magnetopause (Delamere et al., 2011). Additionally, Uranus and Neptune are the planets farthest from the Sun, orbiting at 19.8 AU and 30 AU. They receive the most dilute solar wind density and the weakest interplanetary magnetic field (IMF) in the solar system making them prime environments to study the KHI (Masters, 2018).

In this study, we implemented an analytical model to explore the interaction between the solar wind and the unique geometries presented by the ice giants' magnetospheres. Specifically, we aim to understand the potential for KHI to occur at the magnetopause boundaries of these distant planets and determine the variability of this interaction.
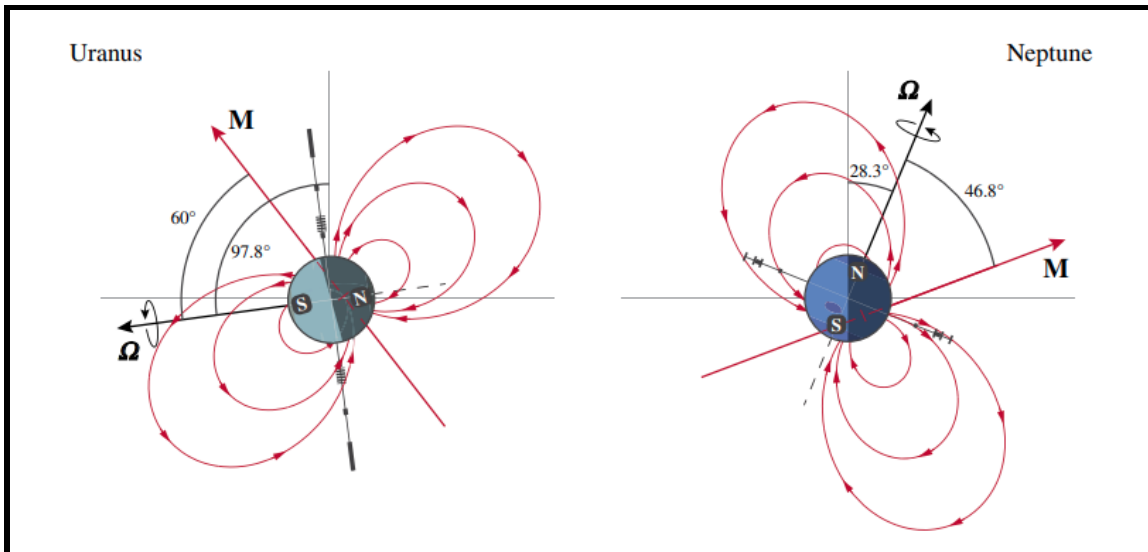
Figure 1. The magnetic and rotational axes of Uranus and Neptune at solstice. Both Uranus' and Neptune's rotations (**Ω**) are counterclockwise. The magnetic axes (**M**) are in red. Although the magnetic dipoles of each planet are measured as offset from the planetary center (as shown in the figure), this offset becomes less influential with increasing distance from the planet, so it is inconsequential for planetary dipole measurements at the magnetopause taken in this study. (Figure from Paty et al., 2020)

II. METHODS

The KHI has been studied at other planets using multi fluid modeling (Zhang et al., 2018), instrument observations (Eriksson et al., 2016), and analytical approaches (Masters, 2018). Since we are limited by a lack of in-situ data at Uranus and Neptune, we have chosen to characterize the nature of the KHI at these ice giant planets using an analytical model of the magnetopause boundary. We applied this analytical model for both the solstice and equinox configurations of Uranus and Neptune's magnetospheres; for each season we examined a range of IMF values and orientations over the course of the planets' rotation. Below we explain the various components and assumptions used to construct the analytical model: the physical geometry of the system, shape of the magnetopause, the k vector, the modeling of solar wind plasma and draped IMF in the magnetosheath, and the assessment of KHI stability.

The analytical model is constructed by creating a magnetopause boundary that separates the shocked solar wind plasma in the magnetosheath from the magnetosphere plasma. The KHI can potentially develop along the magnetopause boundary in regions where the following condition is satisfied:

$$(\boldsymbol{k} \cdot (\boldsymbol{v_1} - \boldsymbol{v_2}))^2 > \frac{1}{\mu_0}(\frac{1}{\rho_1} + \frac{1}{\rho_2})[(\boldsymbol{k} \cdot \boldsymbol{B_1})^2 + (\boldsymbol{k} \cdot \boldsymbol{B_2})^2] \tag{1}$$

where $\boldsymbol{k}$ is the perturbation wave vector along the magnetopause, $\boldsymbol{v_1}$ is the velocity of the shocked solar wind, $\boldsymbol{v_2}$ is the velocity of the magnetospheric plasma, ρ_1 is the shocked solar wind density, ρ_2 is the magnetosphere density, $\boldsymbol{B_1}$ is the IMF carried by the solar wind, and $\boldsymbol{B_2}$ is the planetary magnetic field (Delamere et al., 2011; Chandrasekhar, 1961).

Model Geometry

The model is constructed in a three-dimensional grid space centered at the planet and is defined by the X axis pointing away from the Sun, the Y axis lying in the orbital plane and parallel to the orbital velocity of the planet, and the Z axis completing the right-handed system. Each grid space in any direction is the length of one planetary radii, R_U for one Uranus radii and R_N for one Neptune radii. For Uranus, the model extends -48 R_U to 48 R_U in the Y and Z directions, and -21 R_N to 164 R_N in the X direction. For Neptune, the model extends -47 R_N to 47 R_N in the Y and Z directions, and -27 R_N to 152 R_N in the X directio. We assume the magnetopause at each planet is a paraboloid surface with standoff distances of -20 R_U and -26 R_N, respectively, from the planet which is placed at the origin in the three-dimensional space (Figure 2) (Ness et al. 1986, 1989). Voyager 2 exited Uranus' magnetosphere at around X = 68 R_U and exited Neptune's magnetosphere at around X = 60 R_N (Ness et al., 1986, 1989). We use this information to constrain the model results and do not consider points along the magnetopause

past X = 68 R_U and X = 60 R_N in this paper. All values to the left of the magnetopause boundary in the negative X direction are shocked solar wind values residing in the magnetosheath and all values to the right of the magnetopause are for the planetary magnetosphere.
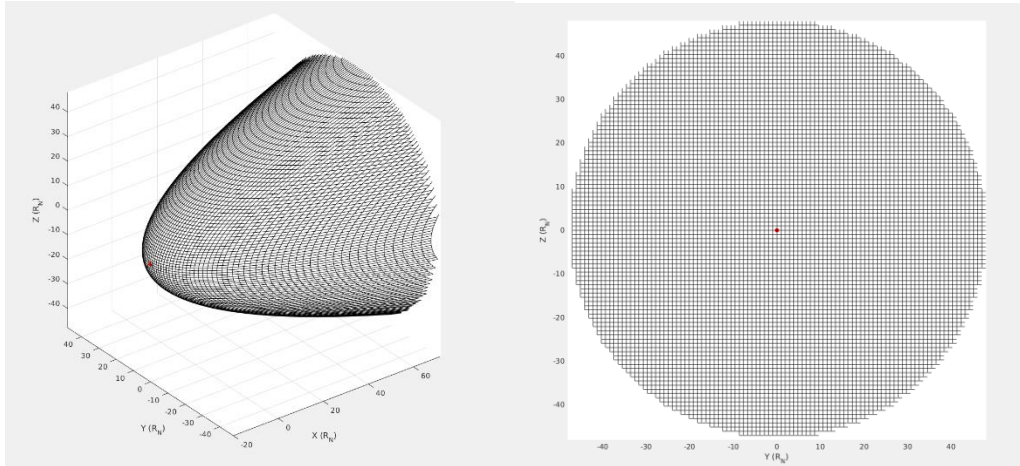

Figure 2. The paraboloid surface representing the magnetopause boundary between the shocked solar wind and planetary magnetosphere exists in a 3D space but has a 2D grid on its curved surface. The magnetopause grid surface is cut off at X = 68 R_U for Uranus and X = 60 R_N for Neptune based on where Voyager 2 exited the planets' magnetospheres. (a) shows the paraboloid in three dimensions and (b) demonstrates how we view results on the paraboloid surface later by looking down the nose of the paraboloid gazing in the X+ direction away from the Sun.

The magnetopause shape and standoff distance are known to vary under different solar wind conditions and a variable planetary magnetic field (Shu et al., 1997, 1998). However, despite the variation of the solar wind conditions and rotation the magnetic phase performed in this study, we chose to hold the paraboloid surface constant for each planet in order to simplify the analysis and enable easier cross-comparison between different solar wind conditions and rotation phases. The paraboloid magnetopause surface is defined in our coordinate system using a modified version of an equation from Cooling et al. (2001):

$$Y^2 + Z^2 = 2R_{MP}(X + R_{MP}) \tag{2}$$

where R_{MP} is the radial distance to the magnetopause. We considered the dayside and nightside (past the dawn-dusk terminator) regions of the magnetopause because the KHI is expected to be more prominent on magnetopause flanks where there is a greater velocity shear between the two plasmas.

Magnetospheric Conditions

We modeled the magnetospheric plasma velocity for both planets by extrapolating from the corotational radial profile observed at Saturn by Cassini and set the plasma velocity to be 80% of the corotational velocity for the radial distance from the planet (Wilson et al., 2009). The magnetospheric plasma travels at this velocity spinning around the planetary rotation axes. The

4

density of Uranus' magnetosphere inside the magnetopause boundary is held at $0.002\ protons/cm^3$ and the density of Neptune's magnetosphere is held at $0.002\ particles/cm^3$ split between hydrogen and nitrogen ions (Sittler et al., 1987, Zhang et al., 1991).

The magnetic field of both planets is represented by a tilted dipole since the quadrupole moment responsible for the apparent "off-centered" dipole source would fall off significantly before reaching the magnetopause boundary of interest. The magnetic vector potential equations were used with the surface magnetic field at the equator to calculate the planetary magnetic field. The surface equatorial magnetic field strength for Uranus is 2.3e-05 T and Neptune is 1.4e-05 T. We applied the analytical model for both solstice and equinox with the magnetic dipole precessing around the rotation axis at a 17.23 hour rotational period for Uranus and a 16.1 hour rotational period for Neptune (Table 1).

Planet and Season	Rotation Axis (from Z axis)	Magnetic Moment Axis (from Z axis)
Uranus - Solstice	97.8 in ZX plane	37.8 in ZX plane
Uranus - Equinox	97.8 in ZY plane	37.8 in ZY plane
Neptune - Solstice	-28.3 in ZX plane	-75.1 in ZX plane
Neptune - Equinox	-28.3 in ZY plane	-75.1 in ZY plane

Table 1. The angles of the rotational and magnetic moment axes for Uranus and Neptune for solstice and equinox at the beginning of their daily rotation. Each model is run for a planet and its season at a set IMF over a planetary rotation. As the planet rotates, we measure if the KHI could occur along the magnetopause boundary between the shocked solar wind and planetary magnetosphere using Equation 1.

Magnetosheath Conditions

The shocked solar wind velocity is determined using equation 1 from Masters (2014):

$$v_{msh} = v_u \sqrt{\frac{(M_s^2+3)}{M_s^2}\left(1 - \left(cos^2\psi + \frac{3^{5/2}}{4^4}\frac{(5M_s^2-1)^{3/2}}{M_s^5}sin^2\psi\right)^{2/5}\right)} \tag{3}$$

Where v_{msh} is the magnetosheath plasma velocity, v_u is the initial solar wind flow speed upstream of the bow shock set at 450 km/s, M_s is the sonic Mach number of the upstream solar wind, and ψ is the flaring angle between the local normal to the magnetopause surface and the x axis.

Although the solar wind density and solar wind are known to be dynamic and variable quantities as they propagate throughout the solar system (Gershman and DiBraccio, 2020), the analytical model is set to be static, and its results represent essentially a snapshot in time with the solar wind density and IMF uniform in space. We held magnetosphere and solar wind density

constant for all the models under various solar wind IMF, ranging two orders of magnitude (0.01, 0.10, 0.30, 0.50 and 1.0 nT) and several IMF orientations (in only Z, only Y, or both Z and Y). We did not consider oppositely oriented IMF magnetic fields in our parameter study due to the square of the dot product between the magnetic fields and k vector in Equation 1. Uranus's magnetosheath density is initially set to $0.030 \; cm^{-3}$ (Sittler et al., 1987) and Neptune's magnetosheath density is initially set to $0.025 \; cm^{-3}$ (Zhang et al., 1991) before further adjustments are made to represent the plasma depletion layer as discussed below.

The magnetic field in the magnetosheath is known to drape and form a tangential discontinuity at the magnetopause surface because of the frozen-in flux theorem (Crooker et al., 1985). The draping geometry of the magnetosheath magnetic field is accounted for by using equations 9-13 of Cooling et al. (2001) that orient the original IMF to curve based on the standoff distances of the bow shock and magnetopause for the planet.

The magnetosheath plasma adjacent to the magnetopause must be adjusted to account for an assumed plasma depletion layer (PDL) of reduced plasma density and enhanced magnetic field strength (Zwan and Wolf, 1976). PDLs have been encountered by spacecraft immediately adjacent to magnetopauses for planets that are closer to the Sun (Anderson et al, 1997; Gershman et al., 2013; Masters et al., 2014). Most planets have an ~85% decrease in local plasma beta in the PDL region (Masters, 2014), which we account for by decreasing the magnetosheath mass density and increasing the magnetosheath magnetic field strength for each point along the magnetopause to produce an 85% reduction in the local plasma beta. Without observational constraints on how far the PDL extends along the magnetopause, we take a conservative approach and assume the PDL extends along the entirety of the magnetopause surface in our model.

KHI Stability

The k vector is the perturbation wave vector along the magnetopause and indicates the direction in which the KHI would propagate. For incompressible plasmas, the phase velocity and group velocity of KH waves are always parallel to the interface. But in a compressible plasma, the component of the perturbation wave vector perpendicular to the interface is purely imaginary meaning that the perturbation is a surface wave at the interface (Pu and Kivelson, 1983b; Masson and Nykyri, 2018).

Stability is possible along the magnetopause based on a range of wave vector k magnitudes that are determined by the lengths of the system. Muira and Pritchett (1982) performed a stability analysis of the Kelvin-Helmholtz Instability in a compressible plasma. However, the wave vector for a compressible plasma has real and imaginary components that cannot be represented in an analytical model such as this one. Although the imaginary component

of the perturbation wave vector was determined from an observed KHI has been witnessed by spacecraft at Earth (Masson and Nykyri, 2018), for the purposes of this model we consider a first order approximation of the k vector by only using real components. Therefore, we consider the simpler case of an incompressible plasma and take a first order approximation of the wave vector as tangential to the magnetopause surface to determine the direction of the vector components (Pu and Kivelson, 1983b). The overall magnitude of k is determined using the condition that $k\Delta < 2$ where Δ is the thickness of the magnetopause boundary (Muira and Pritchett, 1982). The wavenumber $k = \frac{2\pi}{\lambda}$ where the wavelength of the instability λ is limited by the length scales of the magnetosphere system. The gyroradius of the plasma in the PDL is determined to be about 0.01 of a planetary radius (R) when the incoming solar wind is $|B| = 0.01\ nT$ for both planets. This gives both planets a lower bound wavelength of $\lambda = 0.01\ R$ for the KHI to occur, and a corresponding wave vector upper bound of $k = 200$. The thickness of the magnetosheath (5.7 R_U and 8.4 R_N) sets the upper bound on the KHI wavelength for each model, and the wave vector lower bound of 1.1 R_U^{-1} and 0.75 R_N^{-1} (Ness et al., 1986, 1989). The model is confined to using k values:

$$1.1\ R_U^{-1} < k < 200\ R_U^{-1} \tag{4}$$
$$0.75\ R_N^{-1} < k < 200\ R_N^{-1}$$

for instability to occur, based on the application of the length scales of the magnetospheres and using the condition from Muira and Pritchett (1982). The results shown in this paper are for k = 2 R^{-1}.

Magnetosphere and magnetosheath values are taken from either side of the paraboloid surface and used in Equation 1 to evaluate the possibility of the KHI occurring at that point along the magnetopause. We measure the KHI potential along the magnetopause surface multiple times along one rotation for a planetary day and for both the solstice and equinox configurations. The orientation between the vectors in Equation 1 varies as the tilted magnetic dipoles precess around the rotation axis for each icy giant.

Uranus

The results of the model can be interpreted by referring to Equation 1 and how the different parts of the equation change relative to each other over a planetary rotation, a different season, a different incoming IMF. Figure 3 displays the dot product of the wave perturbation vector ($\boldsymbol{k}$) and a set incoming solar wind IMF ($\boldsymbol{B}_1$), the first part of the right side of Equation 1. This value at Uranus changes only when models are run under a different incoming IMF. $\boldsymbol{k} \cdot \boldsymbol{B}_1$ does not vary seasonally or diurnally because both the wave perturbation vector and incoming IMF do not depend on the geometry of the rotating magnetosphere. In comparison, Figure 4 demonstrates what the dot product looks like between the wave perturbation vector ($\boldsymbol{k}$) and the rotating planetary magnetic field ($\boldsymbol{B}_2$) mapped at the magnetopause boundary, and compares this result to the regions where Equation 1 is satisfied resulting in growth of the KHI on Uranus's magnetopause under the same season. For this example, we consider solstice under IMF $B_z = 0.01\ nT$. The similarities in shape and location of the regions of high magnitude ($\boldsymbol{k} \cdot \boldsymbol{B}_2$) and where the KHI is not possible demonstrate Equation 1 in action where the right side of the equation is higher and makes it so the inequality cannot be satisfied i.e., the KHI is not possible in those regions. Understanding ($\boldsymbol{k} \cdot \boldsymbol{B}_1$) is constant for each model run and that ($\boldsymbol{k} \cdot \boldsymbol{B}_2$) evolves as the planet rotates, we can now examine the KHI at Uranus's magnetopause for different seasons.
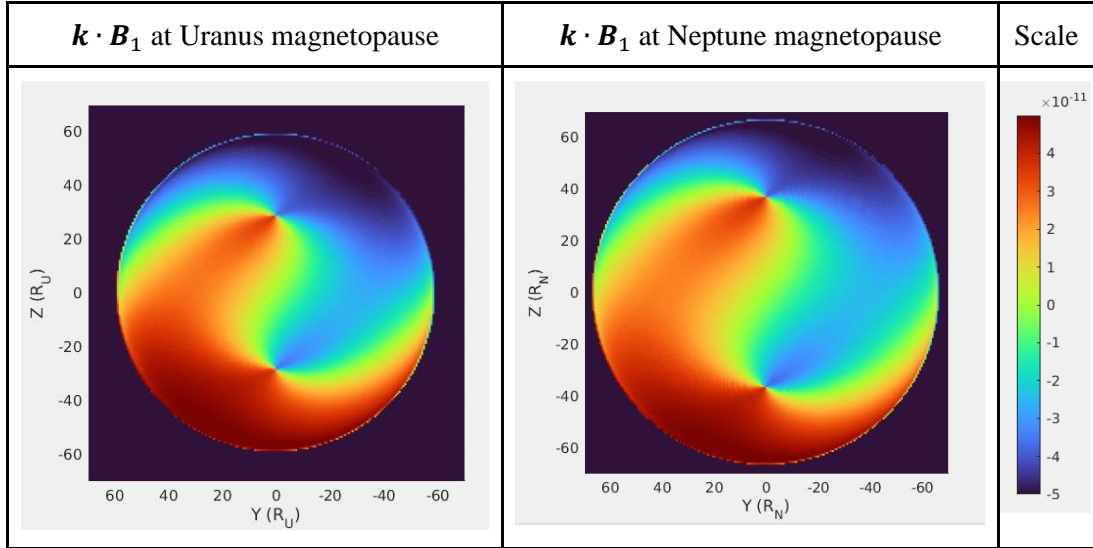
Figure 3. The first part of the right side of Equation 1 is the wave perturbation vector ($\boldsymbol{k}$) dotted with the incoming IMF ($\boldsymbol{B}_1$), which is set to $\boldsymbol{B}_z = 0.01\ nT$ for this example. The wave perturbation vector direction is determined using the slope of the paraboloid surface as a first order approximation. $\boldsymbol{k} \cdot \boldsymbol{B}_1$ is displayed in teslas. The 2D projections of the magnetopause are different sizes because the magnetopauses have different concavities (Equation 2) and different cutoff points in X.

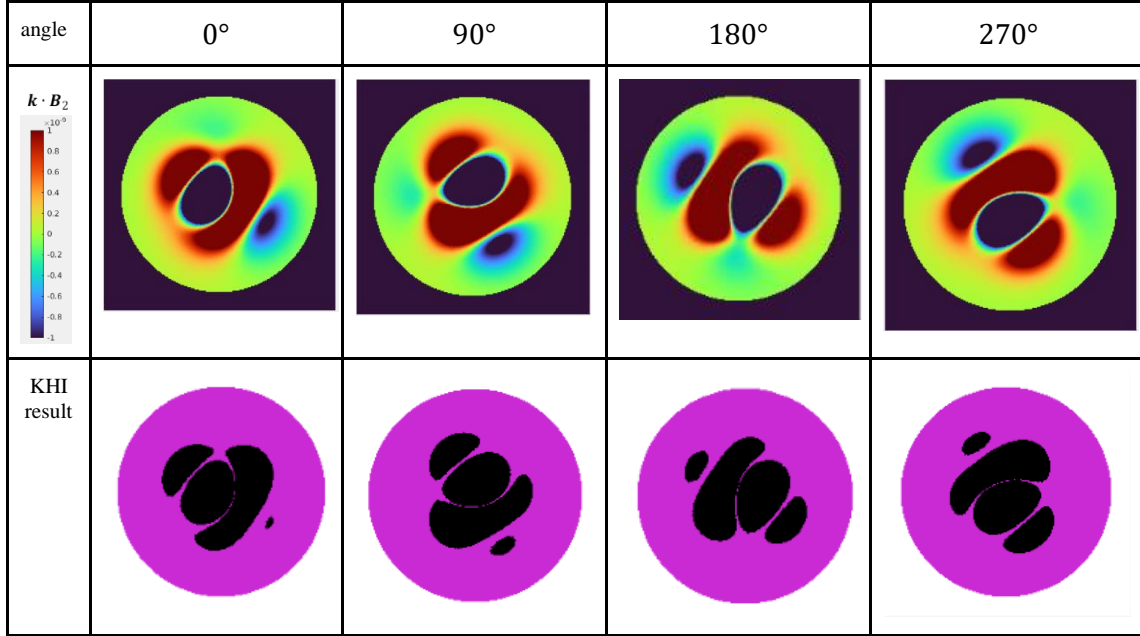**Figure 4.** The second part of the right side of Equation 1 is the dot product of the wave and the planetary magnetic field, which is evaluated at Uranus during solstice for this example and is displayed in the first row over a diurnal rotation in units of teslas. The surface area of Uranus' magnetopause where the KHI is possible is shown in the second row for Uranus at solstice with an incoming IMF of $B_z = 0.01\ nT$. In these figures, magenta indicates where the KHI is possible and black indicates where the KHI is not possible. The side-by-side comparison of $\boldsymbol{k} \cdot \boldsymbol{B}_2$ with the KHI result demonstrates how Equation 1 is primarily controlled by the $\boldsymbol{k} \cdot \boldsymbol{B}_2$ part, when the magnitude of the solar wind IMF is small.

Uranus - Solstice

The first two rows of Figure 5 display regions along Uranus's magnetopause at solstice where the KHI is possible for both low ($0.01\ nT$) and high ($0.50\ nT$) IMF values. The rotation axis is in red and points towards the Sun in the -X direction for the solstice results shown. For the low IMF model results, the KHI is prohibited in the center of the magnetopause in a region that changes over the course of the planetary rotation as the magnetic axis swings around the rotation axis. The KHI results for the low IMF are a direct consequence of the field geometry caused by the ($\boldsymbol{k} \cdot \boldsymbol{B}_2$) term on the right side of Equation 1 and shown in Figure 4. For larger IMF values, the ($\boldsymbol{k} \cdot \boldsymbol{B}_1$) term in Equation 1 is enhanced, suppressing the growth of the KHI over a larger area of the magnetopause than that controlled by the planetary magnetic field via the ($\boldsymbol{k} \cdot \boldsymbol{B}_2$) term. The model results for a higher IMF still prohibit the KHI in the same regions as the low IMF case and additionally prohibit areas along the magnetopause edges (Figure 5). Overall, for both high and low IMF scenarios at solstice the surface area where the KHI is possible at Uranus's magnetopause does not vary significantly.
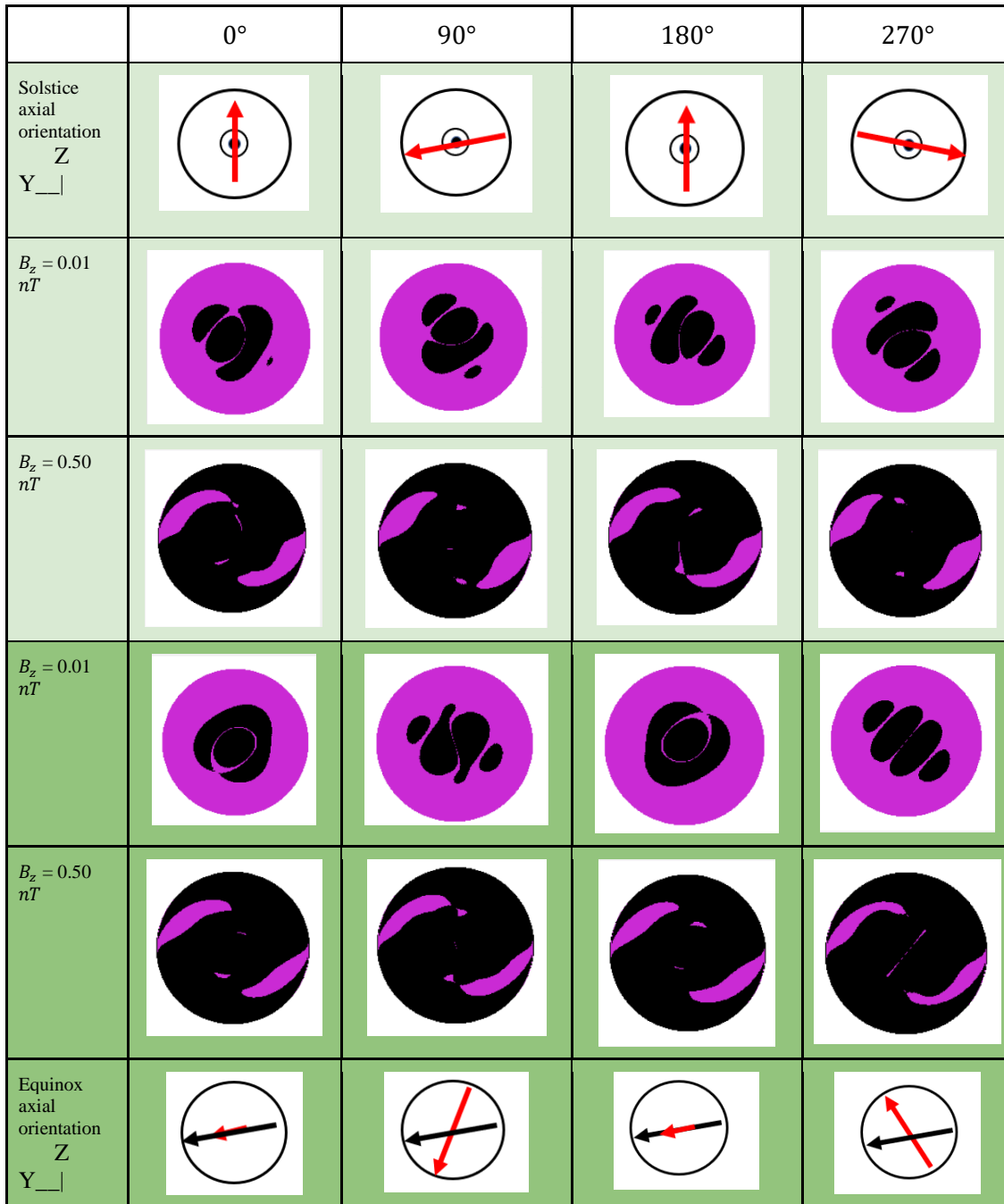
	0°	90°	180°	270°
Solstice axial orientation Z Y__|				
$B_z = 0.01$ nT				
$B_z = 0.50$ nT				
$B_z = 0.01$ nT				
$B_z = 0.50$ nT				
Equinox axial orientation Z Y__|				

Figure 5. At Uranus, the KHI on the surface of the magnetopause is measured for one planetary rotation under incoming solar wind IMF set to low and high values. The first two rows are for Uranus at solstice, and the last two rows are for Uranus at equinox. The regions in magenta indicate where the KHI is possible, and the regions in black indicate where the KHI is not possible on the magnetopause. The axial orientation is shown in the YZ plane at solstice and equinox, with the rotation axis in black and the magnetic axis in red.

Uranus - Equinox

The last two rows in Figure 5 show where the KHI is allowed on Uranus's magnetopause for the same low and high IMF conditions examined for solstice. The low IMF model results for

the Uranus equinox look significantly different from the model results for the Uranus solstice, a result of the rotation axis no longer facing into the Sun. The rotation of the magnetic axis around the rotation axis creates a varying magnetic topology on the magnetopause surface. This topology is reflected in the KHI results for low IMF scenarios, where the regions the KHI is prohibited reflect the same areas where the magnitude of $(\boldsymbol{k} \cdot \boldsymbol{B}_2)$ is high. The results for high IMF for equinox are similar to those for the high IMF solstice scenario, indicating that for high IMF values, the rotating magnetic dipole $(\boldsymbol{B}_2)$ becomes less influential and the regions where the KHI is allowed are determined to be the solar wind IMF strength expressed through the $(\boldsymbol{k} \cdot \boldsymbol{B}_1)$ term in Equation 1.

Uranus - Discussion

The regions where the KHI is allowed in high IMF cases are similar for solstice and equinox indicating that the larger IMF, then $(\boldsymbol{k} \cdot \boldsymbol{B}_1)$ becomes more influential compared to the planetary dipole term $(\boldsymbol{k} \cdot \boldsymbol{B}_2)$. The magnetic geometry of the planetary field is less important in determining where the KHI is allowed for high IMF cases. The low IMF scenarios at both solstice and equinox demonstrate the role of the rotation phase of the magnetic dipole field relative to the magnetopause boundary because the areas where the KHI is prohibited is where low L shells are closest to the magnetopause boundary.

Neptune

The KHI results at Neptune can be analyzed in a similar way as performed for Uranus in the previous section, by quantifying the influence and variability of $(\boldsymbol{k} \cdot \boldsymbol{B}_1)$ and $(\boldsymbol{k} \cdot \boldsymbol{B}_2)$ from Equation 1. However, it is important to recognize that the Neptune models only have the same incoming IMF $(\boldsymbol{B}_1)$ values as the Uranus models. The Neptune model magnetopause is different in size and concavity because the magnetopauses are determined based on the magnetopause standoff distances measured by Voyager 2 and used in Equation 2. This discrepancy can be understood by comparing how $(\boldsymbol{k} \cdot \boldsymbol{B}_1)$ maps onto the magnetopause for each planet. The Neptune magnetopause surface area appears larger when looking down the nose of the magnetopause, but it only appears larger because the flaring angle of the paraboloid is larger than it was for Uranus. The difference in the distribution of $(\boldsymbol{k} \cdot \boldsymbol{B}_1)$ on the surface each planet's magnetopause is not obviously apparent, but the two inflection points of change between negative and positive $(\boldsymbol{k} \cdot \boldsymbol{B}_1)$ are closer to each other at Uranus than at Neptune, which causes a sharper gradient in $(\boldsymbol{k} \cdot \boldsymbol{B}_1)$. Again, the $(\boldsymbol{k} \cdot \boldsymbol{B}_1)$ term remains constant for each season, while the Neptune dipole rotates and interacts with various IMFs for each model run. While transitioning to look at Neptune results, it is also important to remember that the solar wind density is lower. Additionally, the magnetic field strength and obliquity are different at Neptune (Figure 1).
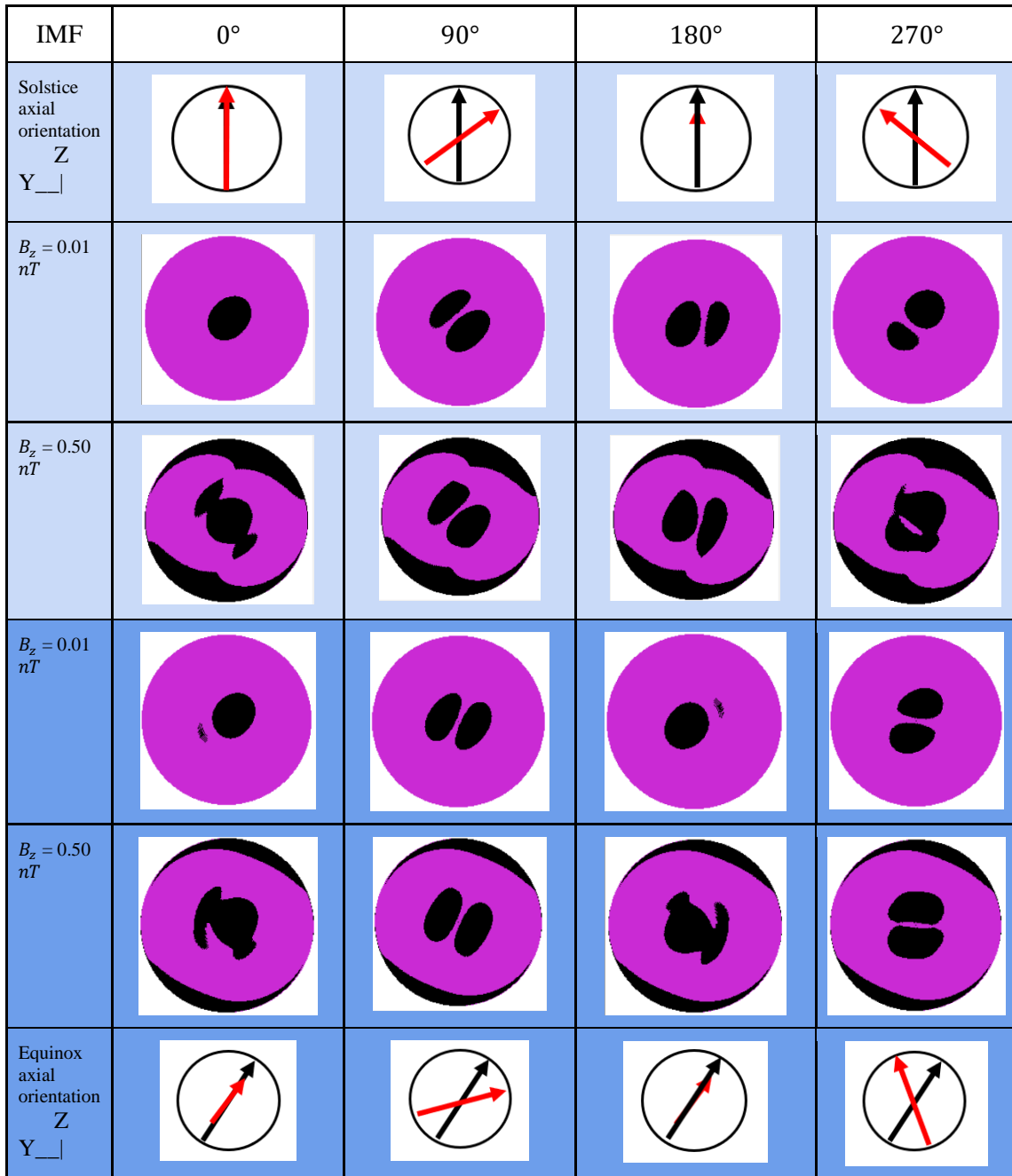
11

IMF	0°	90°	180°	270°
Solstice axial orientation Z Y___|				
$B_z = 0.01$ nT				
$B_z = 0.50$ nT				
$B_z = 0.01$ nT				
$B_z = 0.50$ nT				
Equinox axial orientation Z Y___|				

Figure 6. At Neptune, the KHI on the surface of the magnetopause is measured for one planetary rotation under incoming solar wind IMF set to low and high values. The first two rows are for Neptune at solstice, and the last two rows are for Neptune at equinox. The regions in magenta indicate where the KHI is possible, and the regions in black indicate where the KHI is prohibited on the magnetopause. The axial orientation is shown in the YZ plane at solstice and equinox, with the rotation axis in black and the magnetic axis in red.

Neptune - Solstice

The first two rows of Figure 6 demonstrate the potential for the KHI at Neptune's

magnetopause at solstice for the same low (0.01 nT) and high (0.50 nT) IMF values explored at

Uranus in the previous section. The rotation axis is pointing towards the Sun in the -X direction for solstice. The low IMF case only prohibits the KHI in regions near the nose of the magnetopause. These areas where the KHI is prohibited evolve in size and shape over the course of a planetary rotation, as the dipole precesses around the rotation axis. The high IMF case prohibits the KHI in the same regions as the low IMF, but with additional regions prohibited on the nose and along the magnetopause flanks. This is likely an artifact of the $(\boldsymbol{k} \cdot \boldsymbol{B}_1)$ term being higher in magnitude in those regions of the flanks.

Neptune - Equinox

The KHI results for Neptune at equinox are very similar to the KHI results for Neptune at solstice for both the high and low IMF cases (Figure 6). These similarities are understandable because Neptune's magnetic field orientation relative to the magnetopause doesn't change as drastically as Uranus's magnetic field does between seasons. However, it is notable that the high IMF at Neptune equinox does not prohibit the KHI in as large of surface areas along the flanks of the magnetopause.

Neptune - Discussion

The regions along the magnetopause where the KHI can occur at Neptune look similar for solstice and equinox under the same IMF conditions, implying that seasonality isn't a large factor controlling the favorability of the KHI at Neptune. In comparison to the results for Uranus, Neptune has less area where the KHI is prohibited along the magnetopause flanks for the high IMF models. Overall, there is not much variation in surface area for where the KHI is allowed at Neptune for all IMF conditions explored and for all seasons.

IV. CONCLUSIONS

The surface area trends for the KHI to occur at the magnetopauses of Uranus and Neptune are displayed in Figures 5 and 6, but to understand the variability of the potential for the KHI under different season, diurnal rotation, and IMF values and orientations many more models were run. The likelihood of the KHI to form under these various conditions is presented as the percentage of total magnetopause surface area where the KHI is allowed over the course of one day in Figures 7 and 8. The following conclusions can be made based on the model results.

For low IMF values, the KHI is allowed in constant, large surface areas on the magnetopause over a planetary day. There is little variation in surface area percentage over a planetary rotation for all the modeled seasons and runs IMF values. The KHI is consistently prohibited on the nose of the magnetopause for all IMF values, but the flanks of the magnetopause consistently allow the KHI at low IMF values (Figures 5 and 6) which are more representative and significantly more likely to occur in the outer solar system than 0.3, 0.5, or 1.0 nT cases included in this study.

Under the same solar wind conditions, Neptune is more favorable for the KHI to occur if favorability is considered in terms of the percent of magnetopause surface area that the KHI is allowed (Figures 7 and 8). This conclusion is limited to the conditions of this model where the surfaces we consider the KHI on are different for Uranus and Neptune. The surfaces have different concavities because the equation for the paraboloid surfaces used the standoff magnetopause distances recorded by Voyager 2. The surface areas were also cut off at the points where Voyager 2 exited the magnetopauses at $X = 68\ R_U$ for Uranus and $X = 60\ R_N$ for Neptune.

Changes in magnetic geometry made over the course of a day do not have as big of an influence on the favorability of the KHI as seasonal changes in geometry. The amount of surface area where the KHI is allowed did not vary greatly over the 360° rotation of a planetary day, which can be seen easily as each line is essentially straight across (Figures 7 and 8). In comparison, the same IMF conditions for each planet provided different outcomes for the KHI depending on the season. Solstice is more favorable for the KHI to occur at Uranus, and equinox is more favorable for the KHI to occur at Neptune.

The orientation of the incoming IMF significantly influenced the surface area where the KHI was allowed, which was especially noticeable for stronger IMF magnitudes. For the same magnitude IMF, B_y was the most favorable IMF orientation for the KHI to occur and B_z was the least favorable IMF orientation for the KHI to occur.
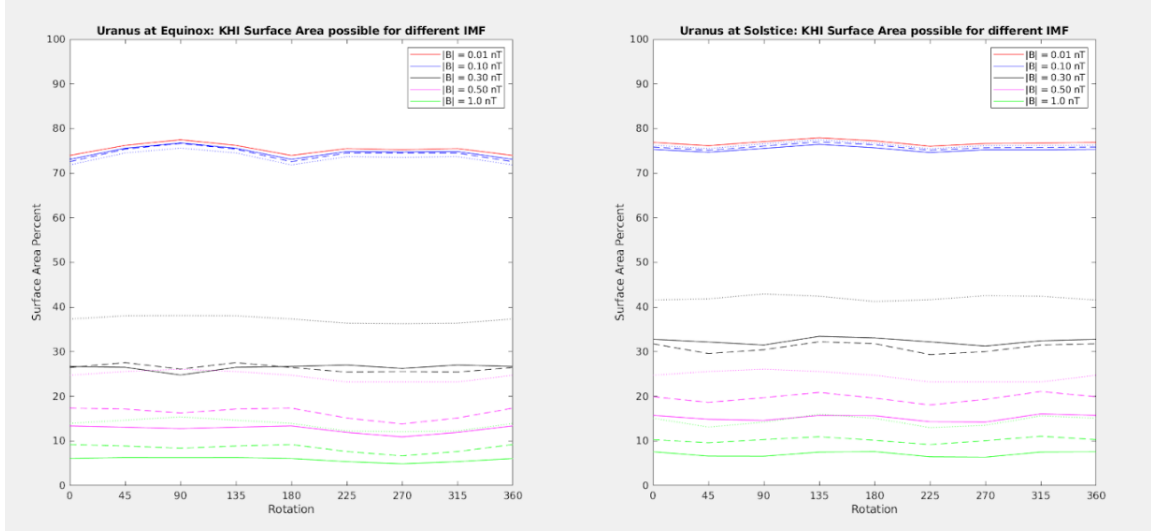
14

Figure 7. The KHI surface area possible at Uranus for (a) solstice and (b) equinox under varying IMF. IMF magnitude is dictated by color with $|B| = 0.01\ nT$ in red, $|B| = 0.10\ nT$ in blue, $|B| = 0.30\ nT$ in black, $|B| = 0.50\ nT$ in magenta, and $|B| = 1.0\ nT$ in green. Solid lines are IMF that is solely B_z, dotted lines are solely B_y, and dashed lines have the IMF split evenly between B_z and B_y to get the $|B|$ magnitude.
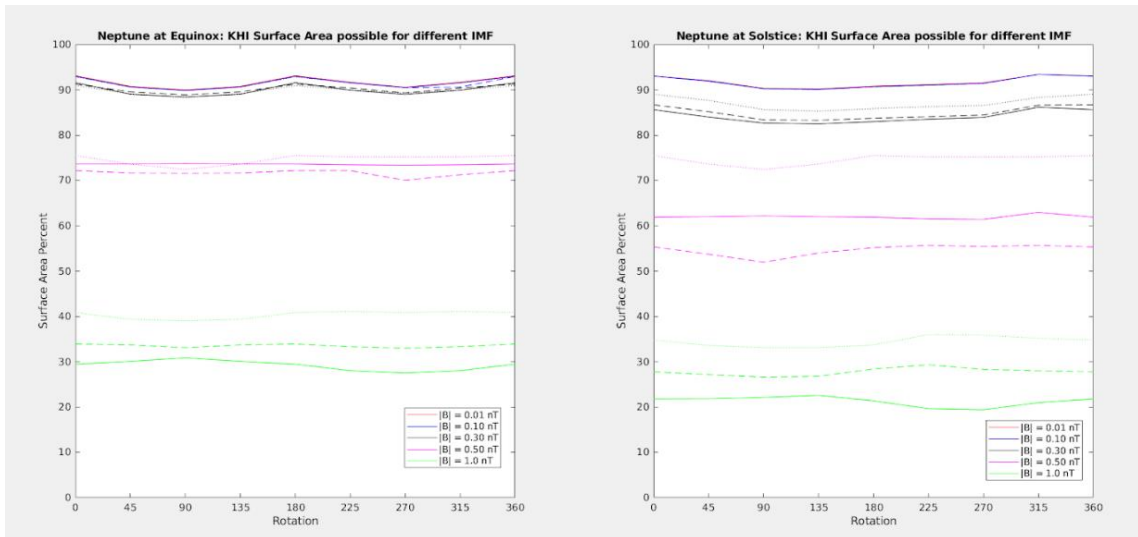

Figure 8. The KHI surface area possible at Neptune for (a) solstice and (b) equinox under varying IMF. IMF magnitude is dictated by color with $|B| = 0.01\ nT$ in red, $|B| = 0.10\ nT$ in blue, $|B| = 0.30\ nT$ in black, $|B| = 0.50\ nT$ in magenta, and $|B| = 1.0\ nT$ in green. Solid lines are IMF that is solely B_z, dotted lines are solely B_y, and dashed lines have the IMF split evenly between B_z and B_y to get the $|B|$ magnitude.

An unanticipated result expressed in the overall trend figures for both Uranus and Neptune was that there seems to be a saturation limit for the KHI surface area allowed for low IMF values. This is particularly evident in the results for IMF values $0.01\ nT$ and $0.10\ nT$ that give essentially the same surface area values at Neptune for both seasons. This KHI surface area

percent limit is a result of the $(\boldsymbol{k} \cdot \boldsymbol{B}_1)$ term on the right side of Equation 1 getting to be insignificantly small such that the $(\boldsymbol{k} \cdot \boldsymbol{B}_2)$ controls the right side of the equation. This limit over the course of a planetary rotation is a characteristic of both planets' magnetic fields, dependent on the surface magnetic field at the equator and the orientation of the magnetic axis relative to the rotation axis.

The results of this analytical model indicate that the ice giants are environments where the Kelvin-Helmholtz Instability may play a more dominant role in controlling the flow of plasma in a magnetosphere. Since this work was done using a static model and merely represented a snapshot in time, future works would apply the same KHI condition (Equation 1) to a dynamic multifluid magnetosphere model and evaluate how the regions where the KHI is allowed and prohibited would evolve as the model itself evolves over time.

REFERENCES CITED

Anderson, B. J., T.-D. Phan, and S. A. Fuselier (1997), Relationships between plasma depletion and subsolar reconnection, J. Geophys. Res., 102, 9531–9542, doi:10.1029/97JA00173.

Axford, W. I. (1964). Viscous interaction between the solar wind and the earth's magnetosphere. *Planetary and Space Science*, *12*(1), 45-53.

Chandrasekhar, S. (1961). Hydrodynamic and hydromagnetic stability. New York: Oxford University Press

Cooling, B. M. A., Owen, C. J., & Schwartz, S. J. (2001). Role of the magnetosheath flow in determining the motion of open flux tubes. *Journal of Geophysical Research: Space Physics*, *106*(A9), 18763-18775.

Crooker, N. U., Luhmann, J. G., Russell, C. T., Smith, E. J., Spreiter, J. R., & Stahara, S. S. (1985). Magnetic field draping against the dayside magnetopause. *Journal of Geophysical Research: Space Physics*, *90*(A4), 3505-3510.

Delamere, P. A., Wilson, R. J., & Masters, A. (2011). Kelvin-Helmholtz instability at Saturn's magnetopause: Hybrid simulations. *Journal of Geophysical Research: Space Physics*, *116*(A10).

Dukes, C. A., Baragiola, R. A., & McFadden, L. A. (1999). Surface modification of olivine by H+ and He+ bombardment. *Journal of Geophysical Research: Planets*, *104*(E1), 1865-1872.

Eriksson, S., Lavraud, B., Wilder, F. D., Stawarz, J. E., Giles, B. L., Burch, J. L., ... & Goodrich, K. A. (2016). Magnetospheric Multiscale observations of magnetic reconnection associated with Kelvin-Helmholtz waves. *Geophysical Research Letters*, *43*(11), 5606-5615.

Futaana, Y., Wieser, G. S., Barabash, S., & Luhmann, J. G. (2017). Solar wind interaction and impact on the Venus atmosphere. *Space Science Reviews*, *212*(3), 1453-1509.

Gershman, D. J., J. A. Slavin, J. M. Raines, T. H. Zurbuchen, B. J. Anderson, H. Korth, D. N. Baker, and S. C. Solomon (2013), Magnetic flux pileup and plasma depletion in Mercury's subsolar magnetosheath, J. Geophys. Res. Space Physics, 118, 7181–7199, doi:10.1002/2013JA019244.

Gershman, D. J., & DiBraccio, G. A. (2020). Solar cycle dependence of solar wind coupling with giant planet magnetospheres. *Geophysical Research Letters*, *47*(24), e2020GL089315.

Lillis, R. J., Brain, D. A., Bougher, S. W., Leblanc, F., Luhmann, J. G., Jakosky, B. M., ... & Lin, R. P. (2015). Characterizing atmospheric escape from Mars today and through time, with MAVEN. *Space Science Reviews*, *195*(1), 357-422.

Masson, A., & Nykyri, K. (2018). Kelvin–Helmholtz instability: Lessons learned and ways forward. *Space Science Reviews*, *214*(4), 1-18.

Masters, A., T. D. Phan, S. V. Badman, H. Hasegawa, M. Fujimoto, C. T. Russell, A. J. Coates, and M. K. Dougherty (2014), The plasma depletion layer in Saturn's magnetosheath, J. Geophys. Res. Space Physics, 119, 121–130, doi:10.1002/2013JA019516.

Masters, A. (2014). Magnetic reconnection at Uranus' magnetopause. *Journal of Geophysical Research: Space Physics*, *119*(7), 5520-5538.

Masters, A. (2018). A more viscous-like solar wind interaction with all the giant planets. *Geophysical Research Letters*, *45*(15), 7320-7329.
McComas, D. J., Elliott, H. A., Weidner, S., Valek, P., Zirnstein, E. J., Bagenal, F., ... & Weaver, H. A. (2016). Pluto's interaction with the solar wind. *Journal of Geophysical Research: Space Physics*, *121*(5), 4232-4246.

Ness, N. F., Acuna, M. H., Behannon, K. W., Burlaga, L. F., Connerney, J. E., Lepping, R. P., & Neubauer, F. M. (1986). Magnetic fields at Uranus. *Science*, *233*(4759), 85-89.

Ness, N. F., Acuna, M. H., Burlaga, L. F., Connerney, J. E., Lepping, R. P., & Neubauer, F. M. (1989). Magnetic fields at Neptune. *Science*, *246*(4936), 1473-1478.

Paty, C., Arridge, C. S., Cohen, I. J., DiBraccio, G. A., Ebert, R. W., & Rymer, A. M. (2020). Ice giant magnetospheres. *Philosophical Transactions of the Royal Society A*, *378*(2187), 20190480.

Poppe, A. R., Sarantos, M., Halekas, J. S., Delory, G. T., Saito, Y., & Nishino, M. (2014). Anisotropic solar wind sputtering of the lunar surface induced by crustal magnetic anomalies. *Geophysical Research Letters*, *41*(14), 4865-4872.

Pu, Z. Y., & Kivelson, M. G. (1983a). Kelvin-Helmholtz instability at the magnetopause: Energy flux into the magnetosphere. *Journal of Geophysical Research: Space Physics*, *88*(A2), 853-861.

Pu, Z. Y., & Kivelson, M. G. (1983b). Kelvin: Helmholtz instability at the magnetopause: Solution for compressible plasmas. *Journal of Geophysical Research: Space Physics*, *88*(A2), 841-852.

Shue, J.-H., J. K. Chao, H. C. Fu, C. T. Russell, P. Song, K. K. Khurana, and H. J. Singer (1997), A new functional form to study the solar wind control of the magnetopause size and shape, J. Geophys. Res., 102, 9497–9511, doi:10.1029/97JA00196.

Shue, J.-H., P. Song, C. T. Russell, J. T. Steinberg, J. K. Chao, G. Gastenker, O. L. Vaisberg, S. Kokubun, H. J. Singer, T. R. Detman, and H. Kawano (1998), Magnetopause location under extreme solar wind conditions, J. Geophys. Res, 103(A8), 17,691–17,700, doi:10.1029/98JA01103.

Sittler Jr, E. C., Ogilvie, K. W., & Selesnick, R. (1987). Survey of electrons in the Uranian magnetosphere: Voyager 2 observations. *Journal of Geophysical Research: Space Physics*, *92*(A13), 15263-15281.

Szalay, J. R., & Horányi, M. (2015). The search for electrostatically lofted grains above the Moon with the Lunar Dust Experiment. *Geophysical Research Letters*, *42*(13), 5141-5146.

Wilson, R. J., Tokar, R. L., & Henderson, M. G. (2009). Thermal ion flow in Saturn's inner magnetosphere measured by the Cassini plasma spectrometer: A signature of the Enceladus torus?. *Geophysical research letters*, *36*(23).

Zhang, M., Richardson, J. D., & Sittler Jr, E. C. (1991). Voyager 2 electron observations in the magnetosphere of Neptune. *Journal of Geophysical Research: Space Physics*, *96*(S01), 19085-19100.

Zhang, B., Delamere, P. A., Ma, X., Burkholder, B., Wiltberger, M., Lyon, J. G., ... & Sorathia, K. A. (2018). Asymmetric Kelvin-Helmholtz instability at Jupiter's magnetopause boundary: Implications for corotation-dominated systems. *Geophysical Research Letters*, *45*(1), 56-63.

Zwan, B. J., and R. A. Wolf (1976), Depletion of solar wind plasma near a planetary boundary, J. Geophys. Res., 81, 1636–1648, doi:10.1029/ JA081i010p01636.